

# Electronic structure and resonant inelastic x-ray scattering in Ta<sub>2</sub>NiSe<sub>5</sub>

D.A. Kukusta,<sup>1</sup> L.V. Bekenov,<sup>1</sup> A.N. Yaresko,<sup>2</sup> K. Ishii,<sup>3</sup> T. Takayama,<sup>2</sup> H. Takagi,<sup>2</sup> and V.N. Antonov<sup>1,2</sup>

<sup>1</sup>*G. V. Kurdyumov Institute for Metal Physics of the N.A.S. of Ukraine,  
36 Academician Vernadsky Boulevard, UA-03142 Kyiv, Ukraine*

<sup>2</sup>*Max-Planck-Institute for Solid State Research, Heisenbergstrasse 1, 70569 Stuttgart, Germany*

<sup>3</sup>*Synchrotron Radiation Research Center, National Institutes for  
Quantum Science and Technology, Sayo, Hyogo 679-5148, Japan*

(Dated: December 23, 2024)

We study the electronic structure of Ta<sub>2</sub>NiSe<sub>5</sub> in its low-temperature semiconducting phase, using resonant inelastic x-ray scattering (RIXS) at the Ta  $L_3$  edge. We also investigate the electronic properties of Ta<sub>2</sub>NiSe<sub>5</sub> within the density-functional theory (DFT) using the generalized gradient approximation in the framework of the fully relativistic spin-polarized Dirac linear muffin-tin orbital band-structure method. While ARPES, dc transport, and optical measurements indicate that Ta<sub>2</sub>NiSe<sub>5</sub> is a small band-gap semiconductor, DFT gives a metallic nonmagnetic solution in Ta<sub>2</sub>NiSe<sub>5</sub>. To obtain the semiconducting ground state in Ta<sub>2</sub>NiSe<sub>5</sub> we use a self-interaction-like correction procedure by introducing an orbital-dependent potential  $V_l$  into the Hamiltonian. We investigate theoretically the x-ray absorption spectroscopy (XAS) and RIXS spectra at the Ni and Ta  $L_3$  edges and analyze the spectra in terms of interband transitions. We also investigate the RIXS spectra as a function of momentum transfer vector  $\mathbf{Q}$  and incident photon energy.

PACS numbers: 75.50.Cc, 71.20.Lp, 71.15.Rf

## I. INTRODUCTION

Transition-metal compounds containing  $5d$  elements usually have a rich variety of novel electronic states emerged from competing interactions, including the on-site Coulomb repulsion  $U$ , crystal-electric field (CEF), and spin-orbit coupling (SOC). These compounds possess the on-site Coulomb repulsion and SOC of the same order of magnitude ( $U \sim 1\text{--}2$  eV,  $\lambda_{SOC} \sim 0.5$  eV) [1]. It can give rise to some fascinating phenomena, such as topological insulators [2–5], Mott insulators [6–10], Weyl semimetals [11–13], and quantum spin liquids [8, 14].

In this paper, we consider the transition-metal chalcogenide Ta<sub>2</sub>NiSe<sub>5</sub>, which has been studied recently in the respect of the possible realization of the excitonic insulator (EI) state [15–17]. This chalcogenide form a quasi-one-dimensional (1D) chain structure with Ni single and Ta double chains running along the  $a$  axis. Along the  $b$  axis the layers are loosely held together by van der Waals' forces [18]. High temperature measurements of resistivity have shown that Ta<sub>2</sub>NiSe<sub>5</sub> is a small band gap semiconductor with quasi-1D anisotropic electron conduction [19]. The nature of the electronic structure of the Ta<sub>2</sub>NiSe<sub>5</sub> orthorhombic phase (space group  $Cmcm$ ) is still strongly debated and this phase is argued to be a semimetal [20–22], almost zero energy gap semiconductor with the energy gap  $\Delta E \leq 0.05$  eV [23], or conventional semiconductor [16, 24, 25]. At critical temperature  $T_c = 328$  K, however, an anomaly in the resistivity occurs, which was associated with the second-order structural phase transition from an orthorhombic to monoclinic phase [17, 19]. The resistivity exhibits insulating behavior both above and below the transition temperature  $T_c$  [24]. The magnetic susceptibility exhibits diamagnetism in a wide temperature range (4.2–900 K) and

shows a sudden drop (being more negative)  $\leq T_c$  [19]. The characteristic energy gap according to optical conductivity and RIXS measurements reaches  $\Delta E \sim 0.16$  eV  $\leq T_c$  [23, 26, 27]. Tunneling spectroscopy estimates the energy gap  $\sim 0.3$  eV at 78 K [22]. ARPES experiments showed that the spectra are strongly temperature dependent [15, 16]. At 40 K the valence band top flattens, the quasiparticle peak sharpens and the size of the band gap becomes larger. It was suggested that the EI state is realized as the ground state of this material, with excitons formed by a charge transfer between the Ni and Ta chains [15, 24, 28]. However, direct evidence of excitons and their behavior across the EI transition has thus far not been reported.

While ARPES, dc transport, and optical measurements indicate that Ta<sub>2</sub>NiSe<sub>5</sub> is a small band-gap semiconductor, density functional theory (DFT) gives a metallic nonmagnetic solution in Ta<sub>2</sub>NiSe<sub>5</sub> [17, 26]. The top of the valence band, formed by (almost) completely occupied Se  $4p$  and Ni  $3d$  states, overlaps with the bottom of the conduction band, which is derived from Ta  $5d$   $t_{2g}$  states hybridized with the chalcogen  $4p$  ones. Thus, according to the DFT calculations the formal valencies are close to Ta<sup>5+</sup> ( $5d^0$ ), Ni<sup>0</sup> ( $3d^{10}$ ), and Se<sup>2-</sup> ( $4p^6$ ). Because Ta<sub>2</sub>NiSe<sub>5</sub> possesses only fully occupied (Ni  $3d$  and Se  $4p$ ) and completely empty (Ta  $5d$ ) shells it cannot be the subject for the application of the LDA+ $U$  method. This method is not able to open up a gap [22, 26]. To reproduce the experimental band gap Kaneko *et al.* [17] introduce a self-interaction-like correction (SIC) procedure [29, 30], where the conduction (valence) bands are shifted upward (downwards) by adding a SIC-like orbital-dependent potential  $V_l$  to the Hamiltonian so as to open up the gap in the band dispersion. The authors add the potentials  $+V_l$  to the energy of the  $5d$  orbitals of Ta and

$-V_l$  to the energy of the  $3d$  orbitals of Ni and  $4p$  orbitals of Se in the orthorhombic structure. They found that the band gap actually opens up for  $V_l = 4.2$  eV. They used the value of  $V_l = 5.0$  eV in their band structure calculations. A similar procedure was used also in Ref. [26] to calculate the electronic structure and optical spectra in monoclinic  $\text{Ta}_2\text{NiSe}_5$ . They found that the best agreement between the theoretically calculated and experimentally measured optical spectra is obtained when applying the orbital-dependent potential  $V_l$  only to the Se  $4p$  states ( $V_{Se4p} = -2.5$  eV).

Ma *et al.* [31] investigate the electronic structure of  $\text{Ta}_2\text{NiSe}_5$  as a promising candidate to a three-dimensional topological excitonic insulator. They obtained the Dirac cone type surface states of the low-temperature monoclinic phase.

Windgätter *et al.* [32] provide extensive first-principles calculations of the electronic structure of  $\text{Ta}_2\text{NiSe}_5$  and  $\text{Ta}_2\text{NiS}_5$  using the DFT as well as  $G_0W_0$  approximations. Authors found very strong gap dependence on the type of exchange correlation potential, the gap is equal to 0.018, 0.120, 0.179, and 0.278 eV for for the Perdew-Burke-Ernzerhof (PBE), mBJ, HSE03, and HSE06 potentials, respectively, with taking into account SOC. In all cases,  $G_0W_0$  approach predicts a bandgap between 0.1 and 0.163 eV, which is in good agreement with the experimental gap of 0.16 eV measured in optics [23, 26, 27]. The temperature dependence of the band structure shows that the bandgap never closes for increasing electronic temperatures but shows the expected renormalization effects of standard semiconductors due to the increased carrier density. They also calculate the phonon dispersion as well as electron-phonon interaction in the compounds.

In the present study, we focus on the electronic structure and resonant inelastic x-ray spectra (RIXS) of  $\text{Ta}_2\text{NiSe}_5$ . RIXS measurements have been successfully performed at the Ni  $L_3$  edge for  $\text{Ta}_2\text{NiSe}_5$  by Monney *et al.* [33]. The authors present a RIXS map as a function of the incident photon energy, measured at the Ni  $L_3$  edge as well as the in-plane momentum  $Q_x$  dispersion with  $\sigma$ -polarized incident light at 30 K. They also present the x-ray absorption spectroscopy (XAS) spectrum measured at the Ni  $L_3$  edge by the total fluorescence yield. They obtained a band gap at the center of the Brillouin zone of  $\sim 0.35$  eV at  $\leq T_c$ . The authors also estimated the effective valence  $m_V$  and conductive  $m_C$  band masses in close vicinity to the Fermi level. These masses were found to be rather large:  $m_V = 0.8m_e$  and  $m_C \sim 0.9\div 1.3m_e$ . Lu *et al.* also measured the RIXS spectra at the Ta and Ni  $L_3$  edges in a small energy interval up to 1.2 eV [27]. Below  $T_c$ , their RIXS energy-momentum map shows a band gap at the Brillouin zone center of  $\sim 0.16$  eV. The authors interpreted the RIXS spectra in terms of the momentum-resolved joint density of states (JDOS) without taking into account corresponding matrix elements.

Although there has been great progress in the RIXS experiments over the past decade, the number of theoretical calculations of RIXS spectra is extremely limited.

The most calculations of the RIXS spectra of various materials have been carried out using the atomic multiplet approach with several adjustable parameters. The question is to what extent DFT is able to reveal the aspects of RIXS spectra. In this paper, we report the experimentally measured RIXS spectrum of  $\text{Ta}_2\text{NiSe}_5$  at the Ta  $L_3$  edge in a wide energy interval as well as a detailed theoretical investigation of the electronic structure and RIXS spectra at the Ta and Ni  $L_3$  edges. The energy band structure of this transition metal chalcogenide was calculated using the fully relativistic spin-polarized Dirac linear muffin-tin orbital band-structure method.

The paper is organized as follows. The crystal structure of  $\text{Ta}_2\text{NiSe}_5$  and computational details are presented in Sec. II. Section III presents the electronic structure of the chalcogenide. In Sec. IV theoretical investigations of the RIXS spectra of  $\text{Ta}_2\text{NiSe}_5$  at the Ni and Ta  $L_3$  edges are presented, and the theoretical results are compared with experimental measurements. Here, we also report the results of the calculations of x-ray absorption spectra at the Ni and Ta  $L_3$  edges. Finally, the results are summarized in Sec. V.

## II. EXPERIMENTAL AND COMPUTATIONAL DETAILS

### A. RIXS

Resonant inelastic x-ray scattering refers to the process where the material first absorbs a photon. The system then is excited to a short-lived intermediate state, from which it relaxes radiatively. In an experiment, one studies the x rays emitted in this decay process. In the direct RIXS process [34] an incoming photon with energy  $\hbar\omega_{\mathbf{k}}$ , momentum  $\hbar\mathbf{k}$  and polarization  $\epsilon$  excites the solid from a ground state  $|g\rangle$  with energy  $E_g$  to the intermediate state  $|I\rangle$  with energy  $E_I$ . During relaxation the outgoing photon with energy  $\hbar\omega_{\mathbf{k}'}$ , momentum  $\hbar\mathbf{k}'$  and polarization  $\epsilon'$  is emitted, and the solid is in the state  $|f\rangle$  with energy  $E_f$ . A valence electron is excited from state  $\mathbf{k}$  to states  $\mathbf{k}'$  with energy  $\hbar\omega = \hbar\omega_{\mathbf{k}} - \hbar\omega_{\mathbf{k}'}$  and momentum transfer  $\hbar\mathbf{q} = \hbar\mathbf{k} - \hbar\mathbf{k}'$ . The RIXS intensity can in general be presented in terms of a scattering amplitude as [34]

$$I(\omega, \mathbf{k}, \mathbf{k}', \epsilon, \epsilon') = \sum_f |T_{fg}(\mathbf{k}, \mathbf{k}', \epsilon, \epsilon', \omega_{\mathbf{k}})|^2 \times \delta(E_f + \hbar\omega_{\mathbf{k}'} - E_g - \hbar\omega_{\mathbf{k}}), \quad (1)$$

where the delta function enforces energy conservation and the amplitude  $T_{fg}(\mathbf{k}, \mathbf{k}', \epsilon, \epsilon', \omega_{\mathbf{k}})$  reflects which excitations are probed and how, for instance, the spectral weights of final state excitations depend on the polarization vectors  $\epsilon$  and  $\epsilon'$  of the incoming and outgoing x-rays, respectively.

Our implementation of the code for the calculation of the RIXS intensity uses Dirac four-component basis func-

tions [35] in the perturbative approach [36]. RIXS is a second-order process, and its intensity is given by

$$I(\omega, \mathbf{k}, \mathbf{k}', \epsilon, \epsilon') \propto \sum_{\mathbf{f}} \left| \sum_{\mathbf{I}} \frac{\langle \mathbf{f} | \hat{H}'_{\mathbf{k}'\epsilon'} | \mathbf{I} \rangle \langle \mathbf{I} | \hat{H}'_{\mathbf{k}\epsilon} | \mathbf{g} \rangle}{E_{\mathbf{g}} - E_{\mathbf{I}}} \right|^2 \times \delta(E_{\mathbf{f}} - E_{\mathbf{g}} - \hbar\omega), \quad (2)$$

where the delta function enforces energy conservation, and the photon absorption operator in the dipole approximation is given by the lattice sum  $\hat{H}'_{\mathbf{k}\epsilon} = \sum_{\mathbf{R}} \hat{\alpha} \epsilon \exp(-i\mathbf{k}\mathbf{R})$ , where  $\hat{\alpha}$  are Dirac matrices. Both  $|\mathbf{g}\rangle$  and  $|\mathbf{f}\rangle$  states are dispersive so the sum over final states is calculated using the linear tetrahedron method [37]. The matrix elements of the RIXS process in the frame of the fully relativistic Dirac LMTO method were presented in our previous publications [38, 39].

### B. Crystal structure

$\text{Ta}_2\text{NiSe}_5$  at high temperature possesses an orthorhombic crystal structure (space group  $Cmcm$ , number 63). The material has a layered structure stacked loosely by a weak van der Waals interaction, and in each layer, Ni single chains and Ta double chains are running along the  $a$  axis of the lattice to form a quasi-one-dimensional (1D) chain structure [18]. At critical temperature  $T_c = 326$  K,  $\text{Ta}_2\text{NiSe}_5$  undergoes a second-order transition from an orthorhombic structure to a structure with a subtle monoclinic distortion and reduced electrical conductivity [18, 19].

Figure 1 shows the monoclinic crystal structure of  $\text{Ta}_2\text{NiSe}_5$  (space group  $C12/c1$ , number 15) [18]. The Ni and Ta atoms are tetrahedrally and octahedrally coordinated by chalcogen atoms, respectively. The polyhedra are combined by sharing edges to form a repeated unit Ta-Ni-Ta. These chains, which stack in the  $a$  direction, are connected via edge-shared octahedra and shared vertices of tetrahedra (Fig. 1). The unit cell contains two such chains displaced by  $a/2$  with respect to each other. The coordination about the Ta and Ni atoms is slightly distorted from ideal geometry (Table I).

The primitive unit cell contains four Ta ions, two Ni ions, and ten Se ions. All Ta and Ni sites are crystallographically equivalent but there are three inequivalent Se sites,  $\text{Se}_1$ ,  $\text{Se}_2$  and  $\text{Se}_3$ . The Ta-Ta inter-chain distances are fairly large  $d_{\text{Ta-Ta}}^{\perp} = 3.903, 3.980$  Å, so that there is no significant Ta-Ta bonding. Around each Ni atom, however, there are four Ta atoms in a square-planar arrangement with very short Ta-Ni distances  $d_{\text{Ta-Ni}} = 2.804, 2.813$  Å. The Ni ions have a tetrahedra  $\text{NiSe}_4$  arrangement with  $d_{\text{Ni-Se}_1} = 2 \times 2.339$  Å,  $d_{\text{Ni-Se}_3} = 2 \times 2.381$  Å. The  $\text{Ta}^{5+}$  cations are surrounded by Se octahedrons with  $d_{\text{Ta-Se}_1} = 2.523, 2.581$  Å  $d_{\text{Ta-Se}_2} = 2.588, 2.661, 2.678$  Å, and  $d_{\text{Ta-Se}_3} = 2.570$  Å interatomic distances. The distance between metals chained along  $x$ :  $d_{\text{Ta-Ta}}^{\parallel} = d_{\text{Ni-Ni}}^{\parallel} = 2 \times 3.496$  Å [18].

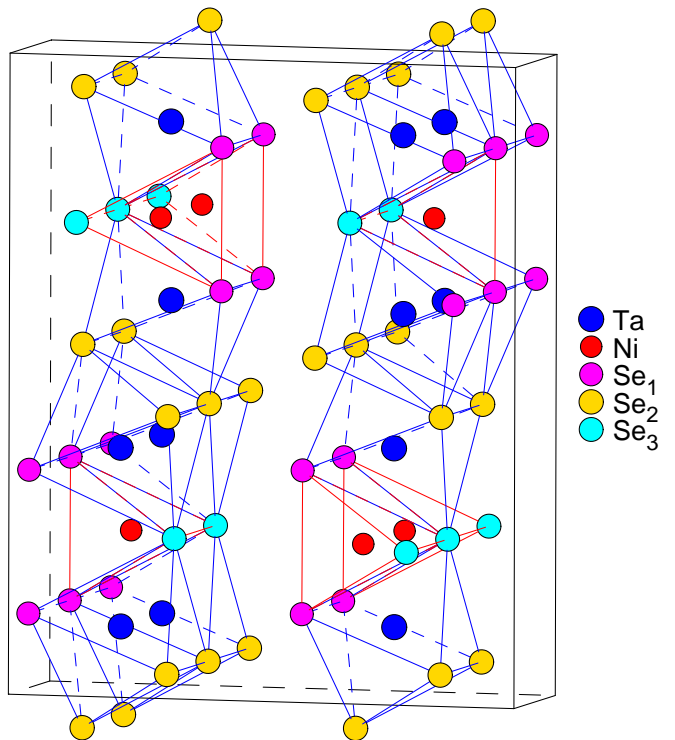


FIG. 1: (Color online) The monoclinic crystal structure of  $\text{Ta}_2\text{NiSe}_5$  (space group  $C12/c1$ , number 15) [18]. Blue and red spheres represent Ta and Ni atoms, respectively, magenta, yellow, and green spheres show Se atoms.

TABLE I: The atomic positions of  $\text{Ta}_2\text{NiSe}_5$ . The lattice constants are equal to  $a = 3.4974$  Å,  $b = 12.8460$  Å and  $c = 15.6457$  Å,  $\beta = 90.0^\circ$  for the orthorhombic crystal structure  $Cmcm$  [21] and  $a = 3.496$  Å,  $b = 12.829$  Å and  $c = 15.641$  Å,  $\beta = 90.530^\circ$  for the monoclinic structure  $C12/c1$  [18].

Structure(Ref.)	Atom	$x$	$y$	$z$
$Cmcm$ [21]	Ta	0.	0.22123	0.11025
	Ni	0.	0.70104	0.25
	$\text{Se}_1$	0.5	0.08037	0.13776
	$\text{Se}_2$	0.	0.14583	0.95074
	$\text{Se}_3$	0.	0.32710	0.25
$C12/c1$ [18]	Ta	-0.00793	0.221349	0.110442
	Ni	0.	0.70113	0.25
	$\text{Se}_1$	0.50530	0.080385	0.137979
	$\text{Se}_2$	-0.00513	0.145648	0.950866
	$\text{Se}_3$	0.	0.32714	0.25

### C. Experimental details

The resonant inelastic x-ray scattering measurement on the Ta  $L_3$ -edge was performed at BL11XU Spring-8. The incident x-ray was monochromatized by a double-crystal Si(111) monochromator and by a secondary 4-bounce Si(333) asymmetric monochromator.  $\pi$ -polarized x-rays with the energy of 9.875 keV were irradiated

onto the ac-plane of the  $\text{Ta}_2\text{NiSe}_5$  crystal, and the horizontally-scattered x-rays were energy-analyzed by a Ge(840) diced analyzer and collected by the Mythen microstrip x-ray detector (Dectris). The total energy resolution was 90 meV. The measurement was performed at a low temperature  $\sim 10$  K.

#### D. Calculation details

The details of the computational method are described in our previous papers [39–42] and here we only mention several aspects. The band structure calculations were performed using the fully relativistic LMTO method [43, 44]. This implementation of the LMTO method uses four-component basis functions constructed by solving the Dirac equation inside an atomic sphere [35]. The exchange-correlation functional of the GGA-type was used in the version of Perdew, Burke and Ernzerhof [45]. The Brillouin zone integration was performed using the improved tetrahedron method [46]. The basis consisted of Ta and Ni  $s$ ,  $p$ ,  $d$ , and  $f$ ; and Se  $s$ ,  $p$ , and  $d$  LMTO's.

It is widely believed that the  $d-d$  excitations show only small momentum transfer vector  $\mathbf{Q}$  dependence in  $5d$  transition metal compounds [47, 48]. However, the soft RIXS spectra in  $3d$  transition metals are more sensitive to the value of  $\mathbf{Q}$ . We used in our RIXS calculations  $\mathbf{Q} = (0.0625, 1.25, 0)$  at the Ni  $L_3$  and  $\mathbf{Q} = (0, 14.5, 0)$  at the Ta  $L_3$  edge, which have been used in the corresponding experimental measurements [33]. We also investigate the dispersion of the RIXS spectra at the Ni and Ta  $L_3$  edges as a function of  $Q_x$ .

The finite lifetime of a core hole was accounted for by folding the spectra with a Lorentzian. The widths of core levels  $\Gamma$  for Ta, Ni, and Se were taken from Ref. [49]. The finite experimental resolution of the spectrometer was accounted for by a Gaussian of 0.6 eV (the  $s$  coefficient of the Gaussian function).

Note that in our electronic structure calculations, we rely on experimentally measured atomic positions and lattice parameters [18, 21] (see Table I) because they are well established for these materials and are probably still more accurate than those obtained from DFT.

It is known that DFT band calculations usually underestimate the band gap in semiconductors [44]. Because  $\text{Ta}_2\text{NiSe}_5$  possesses only fully occupied (Ni  $3d$  and Se  $4p$ ) and completely empty (Ta  $5d$ ) shells the LDA+ $U$  method is not able to open up a gap [22, 26]. To reproduce a semiconducting ground state in  $\text{Ta}_2\text{NiSe}_5$  we used a self-interaction-like correction procedure as it was proposed by Kaneko *et al.* [17], where the conduction (valence) bands are shifted upward (downwards) by adding a SIC-like orbital-dependent potential  $V_i$  to the Hamiltonian. We used  $V_i$  as a parameter and adjusted it to produce the correct value of the band gap and the best agreement with the RIXS experimental spectra.

TABLE II: The theoretically calculated energy gap  $\Delta E$  (in eV) for different  $V_i$ . The experimental energy gap for the low temperature  $C12/c1$  phase was estimated to be  $\sim 0.16$  eV [23, 26, 27].

$V_{\text{Ta}5d}$	$V_{\text{Ni}3d}$	$V_{\text{Se}4p}$	$\Delta E$
0.0	0.0	-2.5	0.0790
0.0	0.0	-4.0	0.1430
0.0	0.0	-5.0	0.1634
0.0	-2.5	-2.5	0.0964
0.0	-4.0	-2.5	0.1123
0.0	-5.0	-2.5	0.1125
0.0	-2.5	-5.0	0.2016
0.0	-4.0	-5.0	0.2282
0.0	-5.0	-5.0	0.2468
2.5	0.0	-2.5	<0
2.5	-2.5	0.0	<0
2.5	-2.5	-2.5	<0
5.0	0.0	-5.0	0.4791
5.0	-5.0	-5.0	0.7907

### III. ELECTRONIC STRUCTURE

We found that  $\text{Ta}_2\text{NiSe}_5$  is a direct-gap semiconductor with the gap minimum at the  $\Gamma$  point of the Brillouin zone in agreement with the experiment [15, 19]. The energy gap for the low temperature  $C12/c1$  phase of  $\sim 0.16$  eV was estimated from optical measurements [23, 26, 27]. Table II presents the theoretically calculated energy gap  $\Delta E$  (in eV) for different  $V_i$  for the low temperature  $C12/c1$  phase.

The shift of Se  $4p$  states is the most important in this case. We found that the best agreement for the band gap in this phase can be achieved for  $V_{\text{Se}4p} = -5.0$  eV with zero values for the other two parameters (see Table II). It should be mentioned that the self-interaction is the interaction of an electron with its own negative density [29, 30]. Thus, it shifts one electron state to higher energies. Therefore, the use of the negative potential shift for the Se  $4p$  and Ni  $3d$  states in order to simulate the self-interaction correction is correct. But the addition of a positive potential shift to the Ta  $5d$  states cannot be justified in the frame of the SIC-like method. Moreover, it worsens the agreement of calculated optical spectra [26] as well as the RIXS spectra (see Fig. 7 below) with experimental measurements. It also cannot produce the correct energy band gap (Table II).

Figure 2 presents the energy band structure and total DOS of monoclinic  $\text{Ta}_2\text{NiSe}_5$  calculated in the fully relativistic Dirac GGA+SO approximation (the top panel) and with taking into account the SIC-like correction ( $V_{\text{Se}4p} = -5.0$  eV) with (red curves) and without (blue curves) SOC (the lower panel). We found that SOC plays a minor role in the electronic structure and band gap value in  $\text{Ta}_2\text{NiSe}_5$ .

Figures 3 and 4 show the energy band structure and partial density of states (PDOS) of monoclinic  $\text{Ta}_2\text{NiSe}_5$

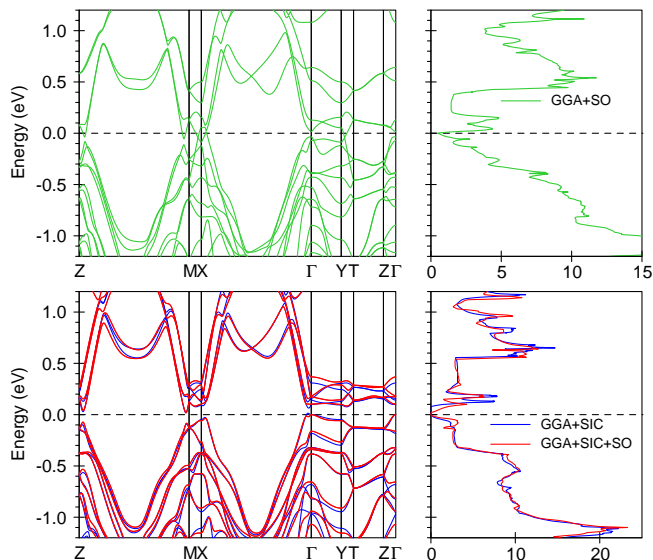


FIG. 2: (Color online) The energy band structure and total density of states (DOS) [in states/(atom eV)] of monoclinic  $\text{Ta}_2\text{NiSe}_5$  calculated in the fully relativistic Dirac GGA+SO approximation (the upper panel, colors represent the dominant orbital character as marked in the legend) and with taking into account the self-interaction-like correction (SIC) ( $V_{\text{Se}4p} = -5.0$  eV) with (red curves) and without (blue curves) SOC (the lower panel).

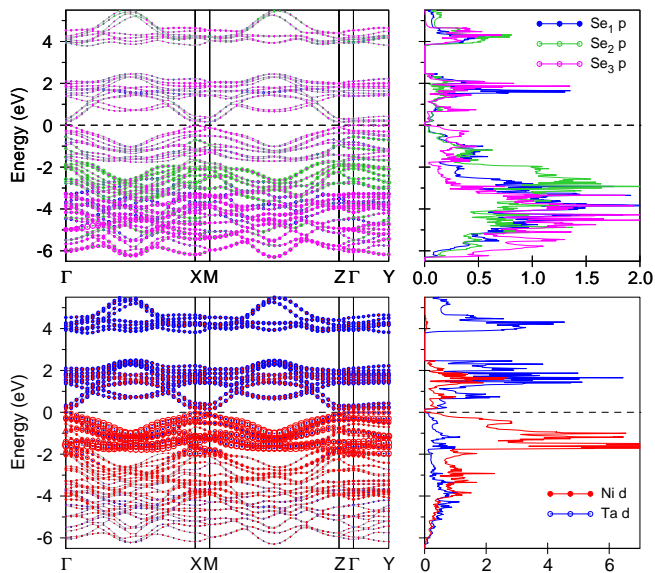


FIG. 3: (Color online) The energy band structure and partial density of states (DOS) of monoclinic  $\text{Ta}_2\text{NiSe}_5$  calculated in the fully relativistic Dirac GGA+SIC+SO approximation ( $V_{\text{Se}4p} = -5.0$  eV). Colors represent the dominant orbital character as marked in the legend.

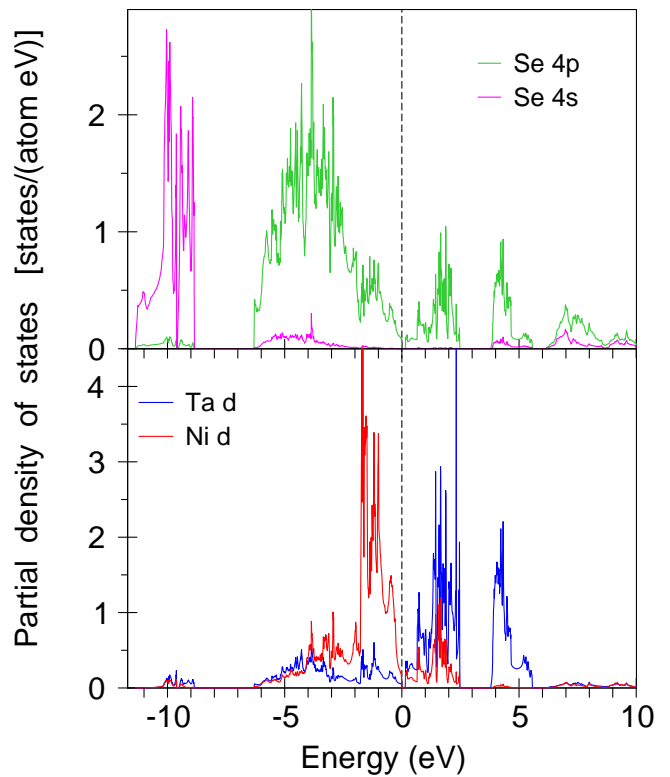


FIG. 4: (Color online) The partial density of states (DOS) of monoclinic  $\text{Ta}_2\text{NiSe}_5$  calculated in the fully relativistic Dirac GGA+SIC+SO approximation ( $V_{\text{Se}4p} = -5.0$  eV).

calculated in the fully relativistic Dirac GGA+SIC+SO approximation ( $V_{\text{Se}4p} = -5.0$  eV). Se 4s states are located from  $-11.4$  to  $-8.85$  eV, Se 4p states occupy a rather large energy interval from  $-6.3$  to  $2.5$  eV and between  $3.8$  and  $10$  eV. They are strongly hybridize with the Ni 3d valent states and Ta 5d conduction states. The fully occupied Ni 3d states are situated between  $-1.9$  eV and  $E_F$ . There are some Ni 3d states at the bottom of the valent band between  $-6.3$  and  $-1.9$  eV, which occur from the strong hybridization with Se 4p states. Ta  $t_2$  states are situated between  $0.16$  and  $2.5$  eV. Ta  $e$  states are separated from the Ta  $t_2$  states by a band gap of  $1.3$  eV and occupy the energy interval from  $3.8$  to  $5.6$  eV. Although formally the Ta valency in  $\text{Ta}_2\text{NiSe}_5$  is close to  $\text{Ta}^{5+}$  ( $5d^0$ ) the occupation number of 5d electrons in the Ta atomic sphere is equal to 2.6. The excessive charge is provided by the tails of Se 4p and Ni 3d states. These  $5d_{\text{Se}}$  and  $5d_{\text{Ni}}$  states play an essential role in the RIXS spectrum at the Ta  $L_3$  edge (see Section V).

#### IV. X-RAY ABSORPTION SPECTRA

Figures 5 and 6 show the theoretically calculated (full blue curves) XAS spectra compared with the experimentally measured spectra at the Ni  $L_3$  [33] and Ta  $L_3$  [27]

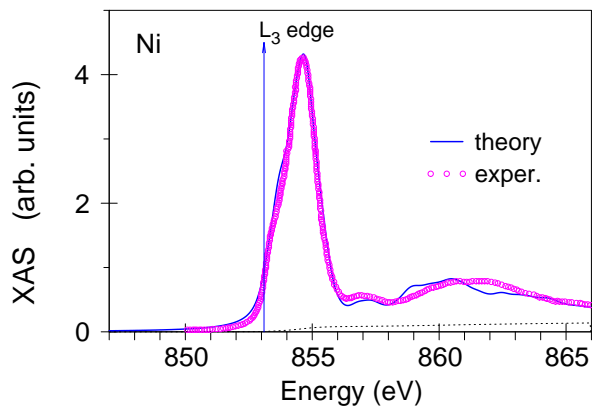


FIG. 5: (Color online) The theoretically calculated (the full blue curve) and experimentally measured [33] (open magenta circles) x-ray absorption spectroscopy (XAS) spectra at the Ni  $L_3$  edge.

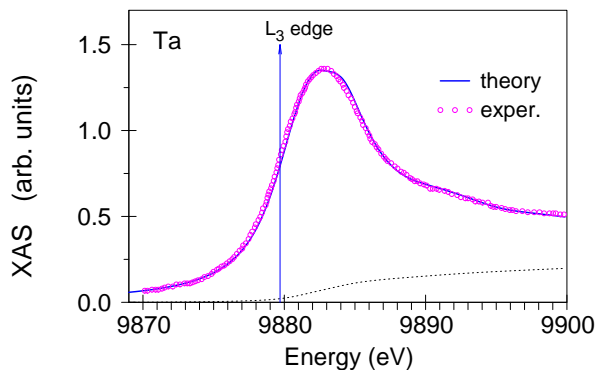


FIG. 6: (Color online) The theoretically calculated (the full blue curve) and experimentally measured [27] (open magenta circles) x-ray absorption spectroscopy (XAS) spectra at the Ta  $L_3$  edge.

edges, respectively. Although Ni  $L_3$  XAS extends more than 15 eV above the edge, the major peak situated at 1.5 eV above the edge is very narrow with a half-width of  $\sim 2$  eV. The peak possesses a low energy shoulder at 0.6 eV above the edge. The spectrum reflects the energy distribution of the Ni  $3d$  states which are located between 0.16 and 2.5 eV (see Fig. 4). The major peak is created by the states situated between 1.2 and 2.5 eV, and the low energy shoulder is due to the states at 0.16–1.0 eV. Ni  $3d$  PDOS is very small above 3.5 eV (see Fig. 4), which leads to relatively small fine structures in Ni  $L_3$  XAS above 856 eV. The peak at 857 eV is due to transitions into the Ni  $3d$  empty states which are derived from the hybridization with Ta  $5d$  states while the fine structures between 859 and 866 eV are due to the hybridization with free electron-like states.

Ta  $L_3$  XAS has an almost four times larger half-width (Fig. 6) in comparison with Ni  $L_3$  XAS because it reflects the energy distribution of the Ta  $t_2$  and  $e$  states situated

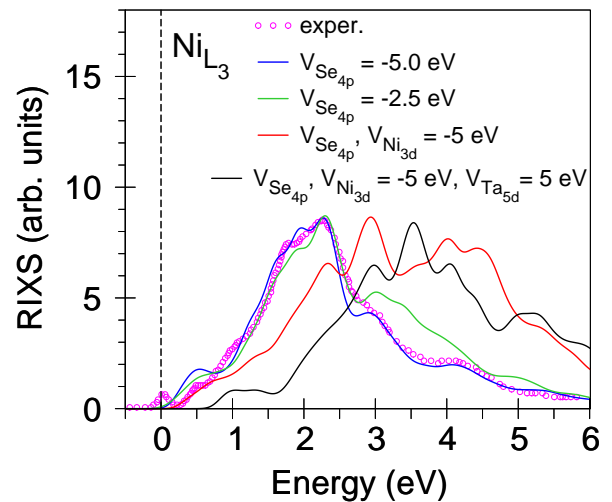


FIG. 7: (Color online) The experimental resonant inelastic x-ray scattering (RIXS) spectrum at the Ni  $L_3$  edge [33] in near-specular geometry  $\mathbf{Q} = (0.0625, 1.25, 0)$  in reciprocal lattice units for incident photon energy  $\hbar\omega_{in} = 853.3$  eV compared with the theoretical RIXS spectra for the same geometry and the incident photon energy calculated in the GGA+SIC+SO approximation for different parameters  $V_l$ .

at 0.16–2.5 eV and 3.8–5.6 eV, respectively. Besides, the width of the Ta  $3p_{3/2}$  core level is much larger than that of Ni  $3p_{3/2}$  (4.68 and 0.47 eV, respectively [49]). The band structure calculations reproduce well the XAS spectra at the Ni and Ta  $L_3$  edges.

## V. RIXS SPECTRA

### A. Ni $L_3$ RIXS spectrum

The experimental RIXS spectrum at the Ni  $L_3$  edge in  $\text{Ta}_2\text{NiSe}_5$  was measured by Monney *et al.* [33] and Lu *et al.* [27] in the energy interval up to 6 and 1.2 eV, respectively. The RIXS spectrum occupies a relatively small energy interval and possesses several fine structures.

Figure 7 presents the influence of the SIC parameter  $V_l$  on the shape of the Ni  $L_3$  RIXS spectrum. We obtained reasonably good agreement with the experiment applying  $V_l$  only to the Se  $4p$  states. Using  $V_{\text{Se}4p} = -2.5$  eV, we describe better the low-energy part of the spectrum, while its high-energy part is described better by  $V_{\text{Se}4p} = -5.0$  eV. Applying the SIC parameter to Ni  $3d$  and/or Ta  $5d$  states makes the agreement with the experiment only worsen.

Figure 8 shows the Ni  $L_3$  RIXS spectrum as a function of incident photon energy above the corresponding edge. We found that the fine structure between 3 and 4 eV is increased with increasing the incident photon energy. It is in qualitative agreement with the corresponding experimental dependence, however, the experiment shows

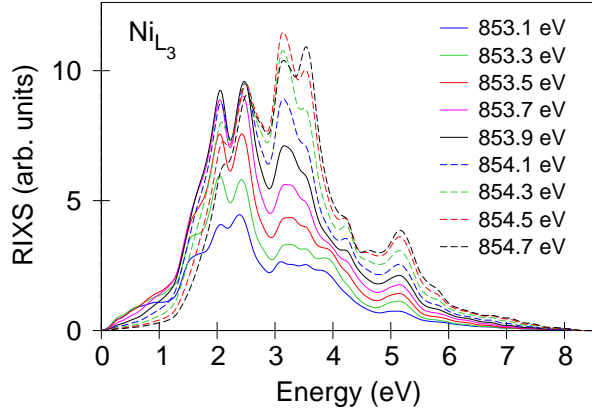


FIG. 8: (Color online) Resonant inelastic x-ray scattering (RIXS) spectra as a function of incident photon energy, calculated at the Ni  $L_3$  edge with momentum transfer vector  $\mathbf{Q} = (0.0625, 1.25, 0)$  in reciprocal lattice units.

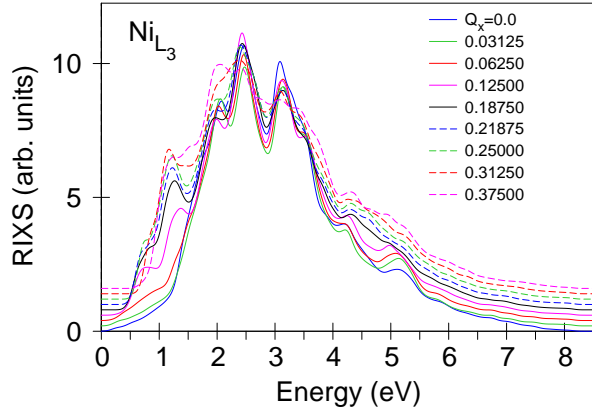


FIG. 9: (Color online) Resonant inelastic x-ray scattering (RIXS) spectra at the Ni  $L_3$  edge calculated as a function of  $Q_x$  in the momentum transfer vector  $\mathbf{Q} = (Q_x, 1.25, 0)$  for incident photon energy  $\hbar\omega_{in} = 853.3$  eV.

weaker dependence [33].

It is widely believed that the  $d-d$  excitations show only small momentum transfer vector  $\mathbf{Q}$  dependence in  $5d$  transition metal compounds [47, 48]. However, the soft RIXS spectra in  $3d$  transition metals are more sensitive to the value of  $\mathbf{Q}$ . Figure 9 shows RIXS spectra at the Ni  $L_3$  edge calculated as a function of  $Q_x$  in  $\mathbf{Q} = (Q_x, 1.25, 0)$  for incident photon energy  $\hbar\omega_{in} = 853.3$  eV. We found that with the increasing of  $Q_x$  the low-energy peak at 1 eV is significantly increased. The fine structure at 2 eV is also increased but to a lesser extent. The similar dependence was also observed experimentally, however, it is weaker in the experiment [33].

The experimentally measured RIXS spectrum consists of a peak centered at zero energy loss, which comprises the elastic line and other low-energy features such as phonons, magnons, etc., and at least six inelastic ex-

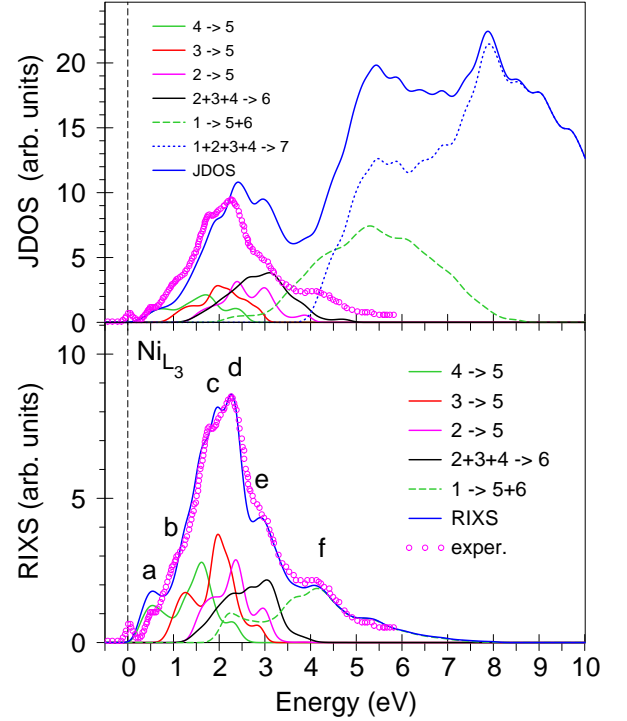


FIG. 10: (Color online) The lower panel: the experimentally measured resonant inelastic x-ray scattering (RIXS) spectrum at the Ni  $L_3$  edge [33] (open magenta circles) in near-specular geometry  $\mathbf{Q} = (0.0625, 1.25, 0)$  for incident photon energy  $\hbar\omega_{in} = 853.3$  eV compared with the theoretical RIXS spectra calculated for the same geometry and incident photon energy in the GGA+SIC+SO approximation with  $V_{Se_{4p}} = -5.0$  eV (the full blue curve) and partial contributions from different interband transitions presented in Fig. 11. The upper panel: joint density of states (JDOS) (the full blue curve) and partial transitions from different interband transitions in comparison with the experimental RIXS spectrum (open magenta circles).

citations. Figure 10 (the lower panel) presents the experimental RIXS spectrum at the Ni  $L_3$  edge [33] (open magenta circles) for  $\mathbf{Q} = (0.0625, 1.25, 0)$  in reciprocal lattice units and incident photon energy  $\hbar\omega_{in} = 853.3$  eV compared with the theoretical RIXS spectrum calculated for the same geometry in the GGA+SIC+SO approximation with  $V_{Se_{4p}} = -5.0$  eV (the full blue curve) and partial contributions from different interband transitions presented in Fig. 11 by different colors. We can divide the Ni  $3d$  valence band in Fig. 11 into two groups. The bands number 1 situated between  $-6.3$  and  $-1.8$  eV are the Ni  $3d_{Se}$  states which are derived from the decomposition of Se  $4p$  states inside the Ni atomic spheres. The bands situated between  $-1.8$  eV and  $E_F$  are Ni  $3d$  states themselves. We divide the latter bands into three groups with numbers from 2 to 4. The empty Ni  $3d$  bands we subdivide into two groups with numbers 5 and 6. We found that the first four fine structures (*a*, *b*, *c*, and *d*) of the Ni  $L_3$  RIXS spectrum are derived from interband transitions from the occupied bands with numbers 2 to 4

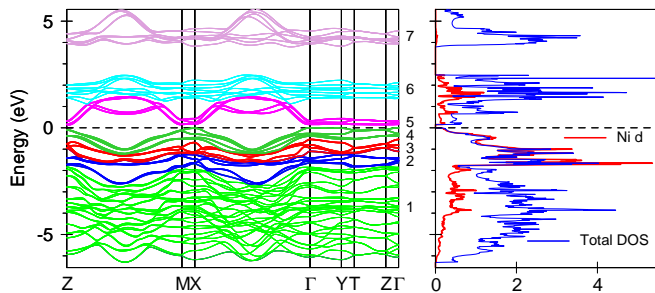


FIG. 11: (Color online) The energy band structure, partial Ni 3d density of states (DOS) [in states/(atom eV)] (the red curve) and normalized total DOS (the blue curve) of monoclinic  $\text{Ta}_2\text{NiSe}_5$  calculated in the fully relativistic Dirac GGA+SIC+SO approximation ( $V_{Se4p} = -5.0$  eV).

4 to the empty bands number 5. The low-energy peak  $a$  is due to interband transition between the closest to the Fermi level bands 4 and 5. The same transitions also contribute to the low-energy shoulder  $c$ . The major peak  $d$  is derived from  $3 \rightarrow 5$  and  $4 \rightarrow 5$  transitions. The high-energy fine structure  $d$  is due to interband transitions from all occupied bands (besides bands 1) to the group of empty bands by number 6. The highest energy structure  $f$  is due to transitions from the Ni  $3d_{Se}$  states (bands 1) to empty states with numbers 5 and 6. It is important to note that all these interband transitions strongly overlap with each other.

Analyzing different interband transitions we found that  $(2+3+4) \rightarrow 5$  transitions are larger than  $(2+3+4) \rightarrow 6$  transitions. RIXS is an element- and orbital-selective X-ray spectroscopy technique, based on a two-step, two-photon resonant process. It combines X-ray emission spectroscopy (XES) with X-ray absorption spectroscopy by measuring the coherent X-ray emission at an incident X-ray photon energy within the near edge X-ray absorption spectrum. In the first step (X-ray absorption) in our case, an electron of the absorbing atom is resonantly excited from a  $2p_{3/2}$  core level into a 5 or 6 empty energy bands. In the second step (X-ray emission), the system radiatively decays from the  $(2+3+4)$  occupied bands into the  $2p_{3/2}$  core level, accompanied by a photon-out emission. Because the X-ray emission is the same for both the cases, we have consider only absorption process into bands 5 and 6 separately. Ref. [42] presents the angular matrix elements for dipole allowed transitions at the  $L_3$  edge from initial core states with different projections  $m_j$  of the total angular momentum  $j = 3/2$  to  $d$  cubic harmonics. It was shown that for the  $\sigma$  incident light the largest contribution is due to  $2p_{3/2} \rightarrow d_{xy}$  and  $2p_{3/2} \rightarrow d_{x^2-y^2}$  transitions (two times larger than the transitions into  $d_{yz}$  and  $d_{xz}$  states and three times larger than the transitions into  $d_{3z^2-1}$  states). Figure 12 presents orbital resolved Ni 3d DOS. The bands number 5 are derived mostly from  $d_{xy}$  orbitals, bands 6 are from  $d_{xz}$ ,  $d_{yz}$ , and  $d_{3z^2-1}$  orbitals. It explains why the  $(2+3+4) \rightarrow 5$

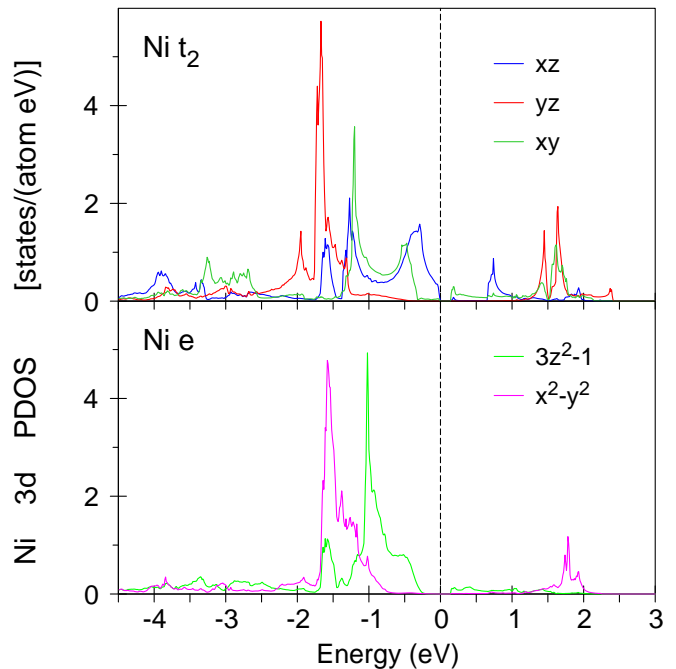


FIG. 12: (Color online) Orbital resolved Ni 3d density of states (DOS) [in states/(atom eV)] of monoclinic  $\text{Ta}_2\text{NiSe}_5$  calculated in the fully relativistic Dirac GGA+SIC+SO approximation ( $V_{Se4p} = -5.0$  eV).

transitions exceed the  $(2+3+4) \rightarrow 6$  ones.

The upper panel of Fig. 10 shows JDOS (the full blue curve) and partial transitions from different interband transitions in comparison with the experimental RIXS spectrum. JDOS is not able to describe correctly the the RIXS spectrum above 2 eV. It can be explained by the difference in the shape of the total and partial Ni 3d DOS presented in Fig. 11 (blue and red curves on the right panel, respectively). We normalized total DOS to Ni PDOS at  $-1.6$  eV. Total DOS of the band group number 1 is significantly larger in comparison with Ni PDOS at the same energy interval. As a result, the intensity of  $1 \rightarrow (5+6)$  transitions is significantly increased for JDOS. Besides, new very intensive transitions  $(1+2+3+4) \rightarrow 7$  appear, which are completely absent in the theoretically calculated RIXS spectrum. The RIXS spectrum at the Ni  $L_3$  edge can be correctly described only with taking into account corresponding matrix elements.

## B. Ta $L_3$ RIXS spectrum

Figure 13 presents the influence of the SIC parameter  $V_i$  on the shape of the Ta  $L_3$  RIXS spectrum. This parameter is less critical than in the Ni  $L_3$  RIXS spectrum. The combination of the parameters  $(V_{Ta5d}, V_{Ni3d}, V_{Se4p}) = (0, -5, -5)$ ,  $(0, 0, -5)$ , and  $(0, 0, -2.5)$  eV give similar Ta  $L_3$  RIXS spectra, although, the last combination produces a slightly better description of the low-energy



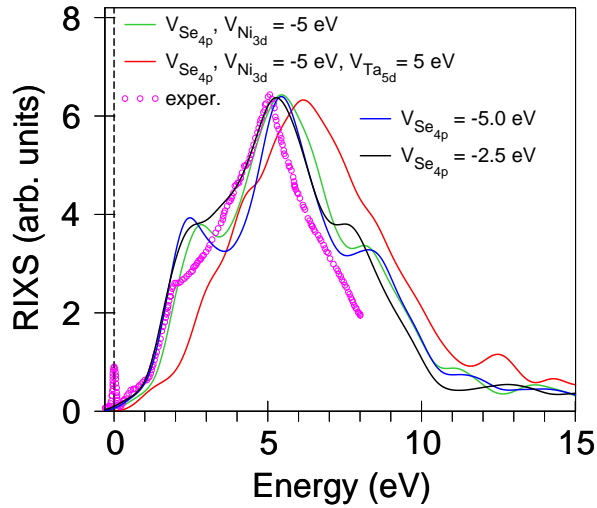


FIG. 13: (Color online) The experimental resonant inelastic x-ray scattering (RIXS) spectrum at the Ta  $L_3$  edge compared with the theoretical RIXS spectra calculated in the GGA+SIC+SO approximation for different parameters  $V_l$ .

shoulder at  $\sim 2.5$  eV. Applying an additional SIC parameter  $V_l$  to the Ta  $5d$  states makes the agreement with the experiment worse.

Figure 14 shows the theoretically calculated RIXS spectra at the Ta  $L_3$  edge as a function of incident photon energy (the upper panel), and as a function of  $Q_x$  in the momentum transfer vector  $\mathbf{Q} = (Q_x, 14.5, 0)$  (the lower panel). RIXS spectrum at the Ta  $L_3$  edge possesses relatively weak dependence from incident photon energy as well as from the momentum transfer vector  $\mathbf{Q}$  in comparison with the corresponding dependences at the Ni  $L_3$  edge (compare Fig. 14 with Figs. 8 and 9). It is in agreement with the Krajewska *et al.* who claimed that the  $d-d$  excitations show only a small momentum transfer vector  $\mathbf{Q}$  dependence in the  $5d$  transition metal compounds [48].

Figure 15 presents the experimental RIXS spectrum at the Ta  $L_3$  edge compared with the theoretically calculated one (the full black curve) and partial contributions from different interband transitions. Because the Ta valency in  $\text{Ta}_2\text{NiSe}_5$  is close to  $\text{Ta}^{5+}$  ( $5d^0$ ) the Ta  $L_3$  RIXS spectrum is formed by a charge transfer between occupied  $5d_{\text{Se}}$  and  $5d_{\text{Ni}}$  states (see Fig. 4) and empty  $t_2$  and  $e$  states (blue and red curves in Fig. 15, respectively). The transitions into the other empty states are very small (the green curve in Fig. 15). Empty total DOS in  $\text{Ta}_2\text{NiSe}_5$  is formed mostly by Ta  $5d$  states, besides, the energy distribution of the occupied part of Ta  $5d$  PDOS, which is formed by the tails of Se  $4p$  and Ni  $3d$  states inside the Ta atomic spheres, repeats the shape of total DOS, therefore, JDOS describes quite well the RIXS spectrum at the Ta  $L_3$  edge (the dotted blue curve in Fig. 15).

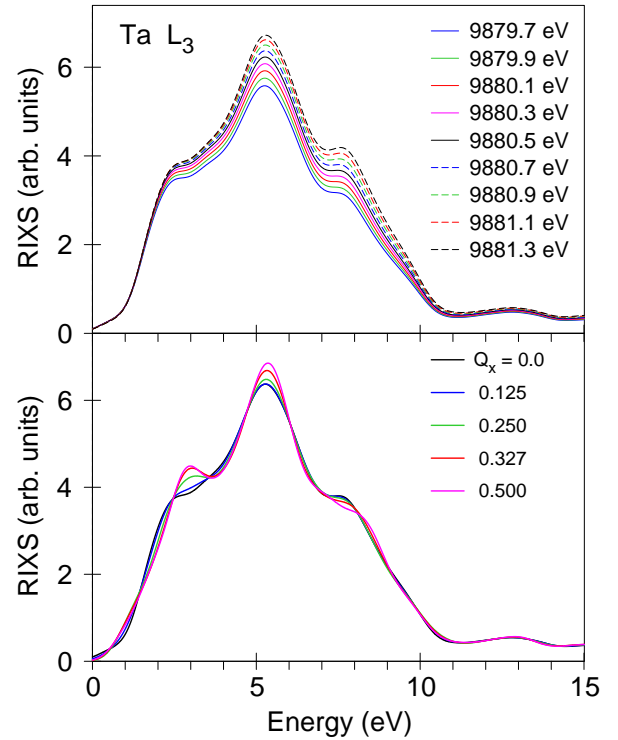


FIG. 14: (Color online) The lower panel: resonant inelastic x-ray scattering (RIXS) spectra at the Ta  $L_3$  edge calculated as a function of  $Q_x$  in the momentum transfer vector  $\mathbf{Q} = (Q_x, 14.5, 0)$  for incident photon energy  $\hbar\omega_{in} = 9679.7$  eV. The upper panel: RIXS spectra as a function of incident photon energy calculated at the Ta  $L_3$  edge with  $\mathbf{Q} = (0, 14.5, 0)$  in reciprocal lattice units.

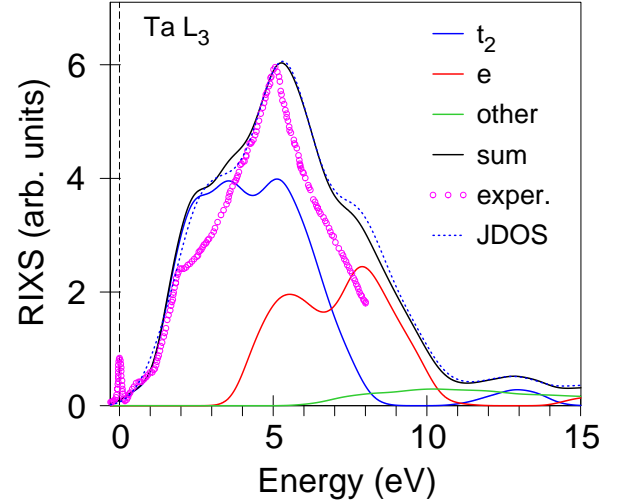


FIG. 15: (Color online) The experimental resonant inelastic x-ray scattering (RIXS) spectrum at the Ta  $L_3$  edge (open magenta circles) compared with the theoretically calculated one (the full black curve) and partial contributions from different interband transitions for the momentum transfer vector  $\mathbf{Q} = (0, 14.5, 0)$  in reciprocal lattice units. The dotted blue curve presents joint density of states (JDOS).

## VI. CONCLUSIONS

The electronic and magnetic properties of quasi-one-dimensional  $\text{Ta}_2\text{NiSe}_5$  were investigated theoretically in the frame of the fully relativistic spin-polarized Dirac LMTO band-structure method. We found that SOC plays a minor role in the electronic structure of  $\text{Ta}_2\text{NiSe}_5$ . The GGA approximation produces a metallic ground state in  $\text{Ta}_2\text{NiSe}_5$  in contradiction with ARPES, dc transport, and optical measurements, which indicate that  $\text{Ta}_2\text{NiSe}_5$  is a small band-gap semiconductor. To obtain the semiconducting ground state in  $\text{Ta}_2\text{NiSe}_5$  we use a SIC-like orbital-dependent potential  $V_l$  incorporated into the Hamiltonian. Although the correct value of the band gap can be achieved using different combinations of the parameters  $V_{Ta5d}$ ,  $V_{Ni3d}$ , and  $V_{Se4p}$ , the shift of Se  $4p$  states is most important in  $\text{Ta}_2\text{NiSe}_5$ . To reproduce the experimental energy gap and get the best agreement between the theory and different experiments we applied the orbital-dependent potential  $V_l$  for the Se  $4p$  states only. We found that the value of  $V_{Se4p}$  is somewhere between  $-2.5$  and  $-5.0$  eV. The value  $V_{Se4p} = -2.5$  eV describes better the low-energy parts of Ni and Ta  $L_3$  RIXS spectra, while the value  $-5.0$  eV describes better the high-energy part of the Ni RIXS spectrum and produces the correct value of the energy band gap.

We investigated experimentally the RIXS spectrum at the Ta  $L_3$  edge and theoretically at the Ni and Ta  $L_3$  edges in  $\text{Ta}_2\text{NiSe}_5$ . The experimentally measured RIXS spectrum at the Ni  $L_3$  edge in addition to the elastic scat-

tering peak at 0 eV possesses several features. We interpret these structures by analyzing particular interband transitions. We investigated the RIXS spectra at the Ni and Ta  $L_3$  edges as a function of momentum transfer vector  $\mathbf{Q}$  and incident photon energy. The RIXS spectrum at the Ta  $L_3$  edge possesses relatively weak dependence on the incident photon energy as well as on the  $\mathbf{Q}$  vector. The RIXS spectrum at the Ni  $L_3$  edge shows a strong increase of the low-energy peak at  $\sim 1$  eV with an increase of the  $Q_x$  component of the vector  $\mathbf{Q}$ . The increase of the incident photon energy  $\hbar\omega_{in}$  above the Ni  $L_3$  edge leads to an increase of the RIXS spectrum in the energy range from 3 to 4 eV.

Empty total DOS in  $\text{Ta}_2\text{NiSe}_5$  is formed mostly by Ta  $5d$  states and the energy distribution of the occupied part of Ta  $5d$  PDOS, which is formed by the tails of the Se  $4p$  and Ni  $3d$  states inside the Ta atomic spheres, repeats the shape of total DOS, therefore, JDOS describes quite well the RIXS spectrum at the Ta  $L_3$  edge. However, the Ni  $L_3$  RIXS spectrum can be correctly described only with taking into account corresponding matrix elements.

## Acknowledgments

RIXS experiments at the Ta  $L_3$ -edge were performed at the BL11XU of SPring-8 with the approval of the Japan Synchrotron Radiation Research Institute (JASRI) (Proposals No. 2016A3552 and No. 2016BA3552).

- 
- [1] W. Witczak-Krempa, G. Chen, Y. B. Kim, and L. Balents, *Annu. Rev. Condens. Matter Phys.* **5**, 57 (2014).
  - [2] X.-L. Qi and S.-C. Zhang, *Physics Today* **63**, 33 (2010).
  - [3] Y. Ando, *J. Phys. Soc. Jpn.* **82**, 102001 (2013).
  - [4] T. O. Wehling, A. Black-Schafferc, and A. Balatsky, *Adv. Phys.* **63**, 1 (2014).
  - [5] A. Bansil, L. H. and T. Das, *Rev. Mod. Phys.* **88**, 021004 (2016).
  - [6] B. J. Kim, H. Jin, S. J. Moon, J.-Y. Kim, B.-G. Park, C. S. Leem, J. Yu, T. W. Noh, C. Kim, S.-J. Oh, et al., *Phys. Rev. Lett.* **101**, 076402 (2008).
  - [7] B. J. Kim, H. Ohsumi, T. Komesu, S. Sakai, T. Morita, H. Takagi, and T. Arima, *Science* **323**, 1329 (2009).
  - [8] G. Jackeli and G. Khaliullin, *Phys. Rev. Lett.* **102**, 017205 (2009).
  - [9] H. Watanabe, T. Shirakawa, and S. Yunoki, *Phys. Rev. Lett.* **105**, 216410 (2010).
  - [10] C. Martins, M. Aichhorn, L. Vaugier, and S. Biermann, *Phys. Rev. Lett.* **107**, 266404 (2011).
  - [11] W. Witczak-Krempa and Y. B. Kim, *Phys. Rev. B* **85**, 045124 (2012).
  - [12] A. Go, W. Witczak-Krempa, G. S. Jeon, K. Park, and Y. B. Kim, *Phys. Rev. Lett.* **109**, 066401 (2012).
  - [13] A. B. Sushkov, J. B. Hofmann, G. S. Jenkins, J. Ishikawa, S. Nakatsuji, S. DasSarma, and H. D. Drew, *Phys. Rev. B* **92**, 241108 (2015).
  - [14] I. Kimchi, J. G. Analytis, and A. Vishwanath, *Phys. Rev. B* **90**, 205126 (2014).
  - [15] Y. Wakisaka, T. Sudayama, K. Takubo, T. Mizokawa, M. Arita, H. Namatame, M. Taniguchi, N. Katayama, M. Nohara, and H. Takagi, *Phys. Rev. Lett.* **103**, 026402 (2009).
  - [16] Y. Wakisaka, T. Sudayama, K. Takubo, T. Mizokawa, N. L. Saini, M. Arita, H. Namatame, M. Taniguchi, N. Katayama, M. Nohara, et al., *J. Supercond. Nov. Magn.* **25**, 1231 (2012).
  - [17] T. Kaneko, T. Toriyama, T. Konishi, and Y. Ohta, *Phys. Rev. B* **87**, 035121 (2013).
  - [18] S. A. Sunshine and J. A. Ibers, *Inorg. Chem.* **24**, 3611 (1985).
  - [19] F. J. DiSalvo, C. H. Chen, R. M. Fleming, J. V. Waszczak, R. G. Dunn, S. A. Sunshine, and J. A. Ibers, *J. Less-Common Met.* **27**, 116 (1986).
  - [20] K. Fukutani, R. Stania, J. Jung, E. F. Schwier, K. Shimada, C. I. Kwon, J. S. Kim, and H. W. Yeom, *Phys. Rev. Lett.* **123**, 206401 (2019).
  - [21] M. D. Watson, I. Markovi, E. A. Morales, P. L. Fevre, M. Merz, A. A. Haghighirad, and P. D. C. King, *Phys. Rev. Res.* **2**, 013236 (2020).
  - [22] J. Lee, C.-J. Kang, M. J. Eom, J. S. Kim, B. I. Min, and H. W. Yeom, *Phys. Rev. B* **99**, 075408 (2019).
  - [23] Y. F. Lu, H. Kono, T. I. Larkin, A. W. Rost,

- T. Takayama, A. V. Boris, B. Keimer, and H. Takagi, *Nat. Commun.* **8**, 14408 (2017).
- [24] K. Seki, Y. Wakisaka, T. Kaneko, T. Toriyama, T. Konishi, T. Suda, N. L. Saini, M. Arita, H. Namatame, M. Taniguchi, et al., *Phys. Rev. B* **90**, 155116 (2014).
- [25] S. Mor, M. Herzog, D. Golez, P. Werner, M. Eckstein, N. Katayama, M. Nohara, H. Takagi, T. Mizokawa, C. Monney, et al., *Phys. Rev. Lett.* **119**, 086401 (2017).
- [26] T. I. Larkin, A. N. Yaresko, D. Pröpper, K. A. Kikoin, Y. F. Lu, T. Takayama, Y.-L. Mathis, A. W. Rost, H. Takagi, B. Keimer, et al., *Phys. Rev. B* **95**, 195144 (2017).
- [27] H. Lu, M. Rossi, J. Kim, H. Yavas, A. Said, A. Nag, M. Garcia-Fernandez, S. Agrestini, K.-J. Zhou, C. Jia, et al., *Phys. Rev. B* **103**, 235159 (2021).
- [28] D. Werdehausen, T. Takayama, M. Höppner, G. Albrecht, A. W. Rost, Y. Lu, D. Manske, H. Takagi, and S. Kaiser, *Science Advances* **4**, 3 (2018).
- [29] J. P. Perdew and A. Zunger, *Phys. Rev. B* **23**, 5048 (1981).
- [30] H. Lin, R. S. Markiewicz, L. A. Wray, L. Fu, M. Z. Hasan, and A. Bansil, *Phys. Rev. Lett.* **105**, 036404 (2010).
- [31] X. Ma, G. Wang, H. Mao, Z. Yuan, T. Yu, R. Liu, Y. Peng, P. Zheng, and Z. Yin, *Phys. Rev. B* **105**, 035138 (2022).
- [32] L. Windgätter, M. Rösner, G. Mazza, H. Hübener, A. Georges, A. J. Millis, S. Latini, and A. Rubio, *NPJ Comp. Mat.* **7**, 210 (2021).
- [33] C. Monney, M. Herzog, A. Pulkkinen, Y. Huang, J. Pellicari, P. Olalde-Velasco, N. Katayama, M. Nohara, H. Takagi, T. Schmitt, et al., *Phys. Rev. B* **102**, 085148 (2020).
- [34] L. J. P. Ament, M. van Veenendaal, T. P. Devereaux, J. P. Hill, and J. van den Brink, *Rev. Mod. Phys.* **83**, 705 (2011).
- [35] V. V. Nemoshkalenko, A. E. Krasovskii, V. N. Antonov, V. N. Antonov, U. Fleck, H. Wonn, and P. Ziesche, *Phys. status solidi B* **120**, 283 (1983).
- [36] E. Arola, P. Strange, and B. L. Gyorffy, *Phys. Rev. B* **55**, 472 (1997).
- [37] G. Lehmann and M. Taut, *Phys. status solidi B* **54**, 469 (1972).
- [38] D. A. Kukusta and A. N. Yaresko, in *Band structure approach to RIXS* (EBS workshop on X-ray Spectroscopy of Magnetic Materials. ESRF, Grenoble, 7–9 October 2019, unpublished).
- [39] V. N. Antonov, D. A. Kukusta, and L. V. Bekenov, *Phys. Rev. B* **105**, 155144 (2022).
- [40] V. N. Antonov, O. Jepsen, A. N. Yaresko, and A. P. Shpak, *J. Appl. Phys.* **100**, 043711 (2006).
- [41] V. N. Antonov, B. N. Harmon, A. N. Yaresko, and A. P. Shpak, *Phys. Rev. B* **75**, 184422 (2007).
- [42] V. N. Antonov, A. N. Yaresko, and O. Jepsen, *Phys. Rev. B* **81**, 075209 (2010).
- [43] O. K. Andersen, *Phys. Rev. B* **12**, 3060 (1975).
- [44] V. Antonov, B. Harmon, and A. Yaresko, *Electronic Structure and Magneto-Optical Properties of Solids* (Kluwer, Dordrecht, 2004).
- [45] J. P. Perdew, K. Burke, and M. Ernzerhof, *Phys. Rev. Lett.* **77**, 3865 (1996).
- [46] P. E. Blöchl, O. Jepsen, and O. K. Andersen, *Phys. Rev. B* **49**, 16223 (1994).
- [47] X. Liu, V. M. Katukuri, L. Hozoi, W.-G. Yin, M. P. M. Dean, M. H. Upton, J. Kim, D. Casa, A. Said, T. Gog, et al., *Phys. Rev. Lett.* **109**, 157401 (2012).
- [48] A. Krajewska, T. Takayama, R. Dinnebier, A. Yaresko, K. Ishii, M. Isobe, and H. Takagi, *Phys. Rev. B* **101**, 121101(R) (2020).
- [49] J. L. Campbell and T. Parr, *At. Data Nucl. Data Tables* **77**, 1 (2001).